

Dated: 28 January 2022

Calibration of Advanced Virgo and Reconstruction of the Gravitational Wave Signal $h(t)$ during the Observing Run O2

F. Acernese^{1,2}, T. Adams³, K. Agatsuma⁴, L. Aiello^{5,6},
A. Allocca^{7,8}, M. A. Aloy⁹, A. Amato¹⁰, S. Antier¹¹,
M. Arène¹², N. Arnaud^{11,13}, S. Ascenzi^{14,15}, P. Astone¹⁶,
F. Aubin³, S. Babak¹², P. Bacon¹², F. Badaracco^{5,6},
M. K. M. Bader⁴, F. Baldaccini^{17,18}, G. Ballardín¹³,
F. Barone^{1,2}, M. Barsuglia¹², D. Barta¹⁹, A. Basti^{7,8},
M. Bawaj^{20,18}, M. Bazzan^{21,22}, M. Bejger²³, I. Belahcene¹¹,
S. Bernuzzi^{24,25}, D. Bersanetti²⁶, A. Bertolini⁴, M. Bitossi^{13,8},
M. A. Bizouard¹¹, S. Bloemen²⁷, M. Boer²⁸, G. Bogaert²⁸,
F. Bondu²⁹, R. Bonnand³, B. A. Boom⁴, V. Boschi¹³,
Y. Bouffanais¹², A. Bozzi¹³, C. Bradaschia⁸, M. Branchesi^{5,6},
T. Briant³⁰, F. Brighenti^{31,32}, A. Brillet²⁸, V. Brisson^{†,11},
T. Bulik³³, H. J. Bulten^{34,4}, D. Buskulic³, C. Buy¹²,
G. Cagnoli^{10,35}, E. Calloni^{36,2}, M. Canepa^{37,26}, P. Canizares²⁷,
E. Capocasa¹², F. Carbognani¹³, J. Casanueva Diaz⁸,
C. Casentini^{14,15}, S. Caudill⁴, F. Cavalier¹¹, R. Cavalieri¹³,
G. Cella⁸, P. Cerdá-Durán⁹, G. Cerretani^{7,8}, E. Cesarini^{38,15},
O. Chaibi²⁸, E. Chassande-Mottin¹², A. Chincarini²⁶,
A. Chiummo¹³, N. Christensen²⁸, S. Chua³⁰, G. Ciani^{21,22},
R. Ciolfi^{39,40}, F. Cipriano²⁸, A. Cirone^{37,26}, F. Cleva²⁸,
E. Coccia^{5,6}, P.-F. Cohadon³⁰, D. Cohen¹¹, A. Colla^{41,16},
L. Conti²², I. Cordero-Carrión⁴², S. Cortese¹³, J.-P. Coulon²⁸,
E. Cuoco¹³, S. D'Antonio¹⁵, V. Dattilo¹³, M. Davier¹¹,
C. De Rossi^{10,13}, J. Degallaix¹⁰, M. De Laurentis^{36,2},
S. Deléglise³⁰, W. Del Pozzo^{7,8}, R. De Pietri^{24,25}, R. De Rosa^{36,2},
L. Di Fiore², M. Di Giovanni^{43,40}, T. Di Girolamo^{36,2},
A. Di Lieto^{7,8}, S. Di Pace^{41,16}, I. Di Palma^{41,16}, F. Di Renzo^{7,8},
V. Dolique¹⁰, M. Drago^{5,6}, M. Eisenmann³, D. Estevez³,
V. Fafone^{14,15,5}, S. Farinon²⁶, F. Feng¹², I. Ferrante^{7,8},
F. Ferrini¹³, F. Fidecaro^{7,8}, I. Fiori¹³, D. Fiorucci¹²,
R. Flaminio^{3,44}, J. A. Font^{9,45}, J.-D. Fournier²⁸, S. Frasca^{41,16},
F. Frasconi⁸, V. Frey¹¹, L. Gammaitoni¹⁷, F. Garufi^{36,2},
G. Gemme²⁶, E. Genin¹³, A. Gennai⁸, V. Germain³, Archisman

Ghosh⁴, B. Giacomazzo^{43,40}, A. Giazotto^{‡,8}, G. Giordano^{1,2},
J. M. Gonzalez Castro^{7,8}, M. Gosselin¹³, R. Gouaty³,
A. Grado^{46,2}, M. Granata¹⁰, G. Greco^{31,32}, P. Groot²⁷,
P. Gruning¹¹, G. M. Guidi^{31,32}, O. Halim^{6,5}, J. Harms^{5,6},
A. Heidmann³⁰, H. Heitmann²⁸, P. Hello¹¹, G. Hemming¹³,
T. Hinderer²⁷, D. Hoak¹³, D. Hofman¹⁰, A. Hreibi²⁸, D. Huet¹¹,
A. Iess^{14,15}, G. Intini^{41,16}, J.-M. Isac³⁰, T. Jacqmin³⁰,
P. Jaranowski⁴⁷, R. J. G. Jonker⁴, S. Katsanevas¹³,
F. Kéfélian²⁸, I. Khan^{5,15}, S. Koley⁴, I. Kowalska³³,
A. Królak^{48,49}, A. Kutynia⁴⁸, A. Lartaux-Vollard¹¹,
C. Lazzaro²², P. Leaci^{41,16}, M. Leonardi⁴⁴, N. Leroy¹¹,
N. Letendre³, A. Longo^{50,51}, M. Lorenzini^{5,6}, V. Lorette⁵²,
G. Losurdo⁸, D. Lumaca^{14,15}, E. Majorana¹⁶, I. Maksimovic⁵²,
N. Man²⁸, M. Mantovani¹³, F. Marchesoni^{20,18}, F. Marion³,
A. Marquina⁴², F. Martelli^{31,32}, L. Martellini²⁸, A. Masserot³,
S. Mastrogiovanni^{41,16}, J. Meidam⁴, L. Mereni¹⁰,
M. Merzougui²⁸, R. Metzdruff³⁰, C. Michel¹⁰, L. Milano^{36,2},
A. Miller^{41,16}, O. Minazzoli^{28,53}, Y. Minenkov¹⁵, M. Mohan¹³,
M. Montani^{31,32}, B. Mours³, I. Nardecchia^{14,15},
L. Naticchioni^{41,16}, G. Nelemans^{27,4}, D. Nichols²⁷,
S. Nissanke^{27,4}, F. Nocera¹³, M. Obergaulinger⁹, G. Pagano^{7,8},
C. Palomba¹⁶, F. Paoletti⁸, A. Paoli¹³, A. Pasqualetti¹³,
R. Passaquieti^{7,8}, D. Passuello⁸, M. Patil⁴⁹, B. Patricelli^{54,8},
R. Pedurand^{10,55}, A. Perreca^{43,40}, O. J. Piccinni^{41,16}, M. Pichot²⁸,
F. Piergiovanni^{31,32}, G. Pillant¹³, L. Pinard¹⁰, R. Poggiani^{7,8},
P. Popolizio¹³, E. K. Porter¹², L. Possenti^{56,32}, G. A. Prodi^{43,40},
M. Punturo¹⁸, P. Puppo¹⁶, P. Rapagnani^{41,16}, M. Razzano^{7,8},
T. Regimbau^{28,3}, L. Rei²⁶, F. Ricci^{41,16}, F. Robinet¹¹,
A. Rocchi¹⁵, L. Rolland³, R. Romano^{1,2}, D. Rosińska^{57,23},
P. Ruggi¹³, L. Salconi¹³, A. Samajdar⁴, N. Sanchis-Gual⁹,
B. Sassolas¹⁰, P. Schmidt²⁷, D. Sentenac¹³, V. Sequino^{14,15,5},
M. Sieniawska²³, A. Singhal^{5,16}, F. Sorrentino²⁶, G. Stratta^{31,32},
B. L. Swinkels⁴, M. Tacca⁴, S. Tiwari^{5,40}, M. Tonelli^{7,8},
A. Torres-Forné⁹, F. Travasso^{13,18}, M. C. Tringali^{43,40},
L. Trozzo^{58,8}, K. W. Tsang⁴, N. van Bakel⁴, M. van Beuzekom⁴,
J. F. J. van den Brand^{34,4}, C. Van Den Broeck^{4,59},
L. van der Schaaf⁴, J. V. van Heijningen⁴, M. Vardaro^{21,22},
M. Vasúth¹⁹, G. Vedovato²², D. Verkindt³, F. Vetrano^{31,32},
A. Viceré^{31,32}, J.-Y. Vinet²⁸, H. Vocca^{17,18}, R. Walet⁴,
G. Wang^{5,8}, M. Was³, A. R. Williamson²⁷, M. Yvert³,
A. Zadrożny⁴⁸, T. Zelenova¹³, J.-P. Zendri²²
(Virgo Collaboration)

S. Kandhasamy^{L1}, A. L. Urban^{L2}

[†]Deceased, February 2018; [‡]Deceased, November 2017.

¹Università di Salerno, Fisciano, I-84084 Salerno, Italy

²INFN, Sezione di Napoli, Complesso Universitario di Monte S. Angelo, I-80126 Napoli, Italy

³Laboratoire d'Annecy de Physique des Particules (LAPP), Univ. Grenoble Alpes, Université Savoie Mont Blanc, CNRS/IN2P3, F-74941 Annecy, France

⁴Nikhef, Science Park 105, 1098 XG Amsterdam, The Netherlands

⁵Gran Sasso Science Institute (GSSI), I-67100 L'Aquila, Italy

⁶INFN, Laboratori Nazionali del Gran Sasso, I-67100 Assergi, Italy

⁷Università di Pisa, I-56127 Pisa, Italy

⁸INFN, Sezione di Pisa, I-56127 Pisa, Italy

⁹Departamento de Astronomía y Astrofísica, Universitat de València, E-46100 Burjassot, València, Spain

¹⁰Laboratoire des Matériaux Avancés (LMA), CNRS/IN2P3, F-69622 Villeurbanne, France

¹¹LAL, Univ. Paris-Sud, CNRS/IN2P3, Université Paris-Saclay, F-91898 Orsay, France

¹²APC, AstroParticule et Cosmologie, Université Paris Diderot, CNRS/IN2P3, CEA/Irfu, Observatoire de Paris, Sorbonne Paris Cité, F-75205 Paris Cedex 13, France

¹³European Gravitational Observatory (EGO), I-56021 Cascina, Pisa, Italy

¹⁴Università di Roma Tor Vergata, I-00133 Roma, Italy

¹⁵INFN, Sezione di Roma Tor Vergata, I-00133 Roma, Italy

¹⁶INFN, Sezione di Roma, I-00185 Roma, Italy

¹⁷Università di Perugia, I-06123 Perugia, Italy

¹⁸INFN, Sezione di Perugia, I-06123 Perugia, Italy

¹⁹Wigner RCP, RMKI, H-1121 Budapest, Konkoly Thege Miklós út 29-33, Hungary

²⁰Università di Camerino, Dipartimento di Fisica, I-62032 Camerino, Italy

²¹Università di Padova, Dipartimento di Fisica e Astronomia, I-35131 Padova, Italy

²²INFN, Sezione di Padova, I-35131 Padova, Italy

²³Nicolaus Copernicus Astronomical Center, Polish Academy of Sciences, 00-716, Warsaw, Poland

²⁴Dipartimento di Scienze Matematiche, Fisiche e Informatiche, Università di Parma, I-43124 Parma, Italy

²⁵INFN, Sezione di Milano Bicocca, Gruppo Collegato di Parma, I-43124 Parma, Italy

²⁶INFN, Sezione di Genova, I-16146 Genova, Italy

²⁷Department of Astrophysics/IMAPP, Radboud University Nijmegen, P.O. Box 9010, 6500 GL Nijmegen, The Netherlands

²⁸Artemis, Université Côte d'Azur, Observatoire Côte d'Azur, CNRS, CS 34229, F-06304 Nice Cedex 4, France

²⁹Univ Rennes, CNRS, Institut FOTON - UMR6082, F-3500 Rennes, France

³⁰Laboratoire Kastler Brossel, Sorbonne Université, CNRS, ENS-Université PSL, Collège de France, F-75005 Paris, France

³¹Università degli Studi di Urbino 'Carlo Bo,' I-61029 Urbino, Italy

³²INFN, Sezione di Firenze, I-50019 Sesto Fiorentino, Firenze, Italy

³³Astronomical Observatory Warsaw University, 00-478 Warsaw, Poland

³⁴VU University Amsterdam, 1081 HV Amsterdam, The Netherlands

³⁵Université Claude Bernard Lyon 1, F-69622 Villeurbanne, France

- ³⁶Università di Napoli 'Federico II,' Complesso Universitario di Monte S. Angelo, I-80126 Napoli, Italy
- ³⁷Dipartimento di Fisica, Università degli Studi di Genova, I-16146 Genova, Italy
- ³⁸Museo Storico della Fisica e Centro Studi e Ricerche "Enrico Fermi", I-00184 Roma, Italy
- ³⁹INAF, Osservatorio Astronomico di Padova, I-35122 Padova, Italy
- ⁴⁰INFN, Trento Institute for Fundamental Physics and Applications, I-38123 Povo, Trento, Italy
- ⁴¹Università di Roma 'La Sapienza,' I-00185 Roma, Italy
- ⁴²Departamento de Matemáticas, Universitat de València, E-46100 Burjassot, València, Spain
- ⁴³Università di Trento, Dipartimento di Fisica, I-38123 Povo, Trento, Italy
- ⁴⁴National Astronomical Observatory of Japan, 2-21-1 Osawa, Mitaka, Tokyo 181-8588, Japan
- ⁴⁵Osservatori Astronòmic, Universitat de València, E-46980 Paterna, València, Spain
- ⁴⁶INAF, Osservatorio Astronomico di Capodimonte, I-80131, Napoli, Italy
- ⁴⁷University of Białystok, 15-424 Białystok, Poland
- ⁴⁸NCBJ, 05-400 Świerk-Otwock, Poland
- ⁴⁹Institute of Mathematics, Polish Academy of Sciences, 00656 Warsaw, Poland
- ⁵⁰Dipartimento di Fisica, Università degli Studi Roma Tre, I-00154 Roma, Italy
- ⁵¹INFN, Sezione di Roma Tre, I-00154 Roma, Italy
- ⁵²ESPCI, CNRS, F-75005 Paris, France
- ⁵³Centre Scientifique de Monaco, 8 quai Antoine Ier, MC-98000, Monaco
- ⁵⁴Scuola Normale Superiore, Piazza dei Cavalieri 7, I-56126 Pisa, Italy
- ⁵⁵Université de Lyon, F-69361 Lyon, France
- ⁵⁶Università degli Studi di Firenze, I-50121 Firenze, Italy
- ⁵⁷Janusz Gil Institute of Astronomy, University of Zielona Góra, 65-265 Zielona Góra, Poland
- ⁵⁸Università di Siena, I-53100 Siena, Italy
- ⁵⁹Van Swinderen Institute for Particle Physics and Gravity, University of Groningen, Nijenborgh 4, 9747 AG Groningen, The Netherlands
- ^{L1}LIGO Livingston Observatory, Livingston, LA 70754, USA
- ^{L2}LIGO, California Institute of Technology, Pasadena, CA 91125, USA

Abstract. In August 2017, Advanced Virgo joined Advanced LIGO for the end of the O2 run, leading to the first gravitational waves detections with the three-detector network. This paper describes the Advanced Virgo calibration and the gravitational wave strain $h(t)$ reconstruction during O2. The methods are the same as the ones developed for the initial Virgo detector and have already been described in previous publications; this paper summarizes the differences and emphasis is put on estimating systematic uncertainties. Three versions of the $h(t)$ signal have been computed for the Virgo O2 run, an online version and two post-run reprocessed versions with improved detector calibration and reconstruction algorithm. A photon calibrator has been used to establish the sign of $h(t)$ and to make an independent partial cross-check of the systematic uncertainties. The uncertainties reached for the latest $h(t)$ version are 5.1% in amplitude, 40 mrad in phase and 20 μ s in timing.

Contents

1 Introduction 5

2 The Advanced Virgo detector during O2 7

2.1 Mirror longitudinal actuation 7

2.2 Sensing of the interferometer output power and control loops 8

3 Calibration of Advanced Virgo 8

3.1 Timing and Sensing 9

3.2 Calibration of the BS, NI and WI mirror actuators 10

3.3 Calibration of the NE and WE mirror actuators 11

3.4 Calibration of the marionnetta actuators 11

3.5 Calibration of the PR mirror actuator 12

3.6 Uncertainties estimation 12

4 Reconstruction of the gravitational wave signal $h(t)$ 14

4.1 Principle 14

4.2 Main differences between the $h(t)$ versions 14

4.3 Uncertainty budget 15

5 Consistency checks with the photon calibrator (PCal) 17

5.1 Principle of the photon calibrator 18

5.2 Sign of $h(t)$ 18

5.3 Partial confirmation of $h(t)$ systematic uncertainties with the PCal . . . 18

6 Conclusion 20

1. Introduction

The Advanced Virgo detector [1, 2] is located near Pisa (Italy) and is looking for gravitational waves sources emitted by astrophysical compact sources in the frequency range 10 Hz to a few kHz. Advanced Virgo joined the two LIGO detectors [3, 4] at the end of the O2 observation run, from 1st to 26th August 2017. The data of all the detectors have been used together to search for gravitational wave sources. During this run, GW170814 [5] was the first gravitational wave event from a binary black hole coalescence detected by the three detectors and GW170817 [6, 7] was the first gravitational wave signal detected from a binary neutron star coalescence.

The Advanced Virgo optical configuration for O2 was that of a power-recycled interferometer with 3 kilometer long Fabry-Perot cavities in the arms. Signal recycling was not implemented yet.

The gravitational wave strain couples to the longitudinal length degree of freedom of the interferometer. But, to operate the interferometer, the relative positions of the different

mirrors are controlled within tight limits [1]. The control extends to a few hundred hertz and modifies the interferometer response to gravitational wave in that bandwidth. Above a few hundred hertz, the suspended mirrors behave as free falling masses around their position: the main effect of a passing gravitational waves is a frequency-dependent variation of the power at the output of the interferometer, following the interferometer optical response.

The main purpose of the Virgo calibration is to allow to reconstruct the amplitude $h(t)$ of the gravitational wave strain from the interferometer data. In the long wavelength approximation, the differential length of the interferometer arms, $\Delta L = L_x - L_y$, is related to the gravitational wave strain h by:

$$h = \frac{\Delta L}{L_0} \quad \text{where} \quad L_0 = 3 \text{ km} \quad (1)$$

For coherent search of gravitational waves with multiple detectors, the sign of $h(t)$ must be well defined across detectors. For Virgo, L_x and L_y respectively stand for the North and the West arm lengths.

Generally speaking, in the $h(t)$ reconstruction, we remove from the dark fringe signal the contributions of the controls signals by subtracting the corrections applied to the mirrors and we correct for the interferometer optical response transfer function. Hence, the responses of the mirror longitudinal actuators have to be calibrated, as well as the readout electronics of the output power and the interferometer optical response. Absolute timing is also a critical parameter for multi-detector analysis, in particular to determine the direction of the gravitational wave source in the sky, by using the time of flight between gravitational wave detectors. Since the typical timing accuracy is on the order of 0.1 ms [8], absolute timing precision must be of the order of tens microseconds or less.

The scope of this paper is to give an overview of the Advanced Virgo calibration and $h(t)$ reconstruction during the run O2, and to describe the systematic uncertainties. The principle of the calibration and reconstruction is still the same as the one developed for the initial Virgo detector and already described in [9] and [10]. The methods are thus not described again in detail in this paper. In section 2, we briefly give an overview of the Virgo detector components that are relevant for calibration during O2, emphasizing the differences with respect to the initial Virgo. In section 3, we describe the calibration of the photodiode readout and mirror actuation. More details are given for the procedures that were modified since initial Virgo, and the systematic uncertainties of each calibration step are provided. Section 4 shows how the $h(t)$ values have been reconstructed using the parameters, delays and transfer functions determined by the calibration. We also describe the different validation checks done on the reconstructed $h(t)$ channel and how they were used to estimate the systematic uncertainties in terms of amplitude, phase and timing.

For O2, three versions of the $h(t)$ reconstruction have been performed: (i) the "Online" reconstruction used during O2 to provide $h(t)$ with a latency of about 20 s to the low-latency gravitational wave searches that triggered alerts to our multi-messengers

partners. This online reconstruction was based on the calibration parameters estimated with the data taken before the start of O2. (ii) a first reprocessing, "V1O2Repro1A"[‡] which was run in September 2017 with improved calibration parameters determined using calibration data taken during and after O2 and an improved reconstruction algorithm. This version was used for the first O2 papers with Virgo data published in Fall 2017 and in [7]. (iii) a second reprocessing, "V1O2Repro2A", which was run in January 2018 with finely tuned calibration models and further improvements of the reconstruction algorithm. The results shown in this paper pertain to the final actuator calibration and to the second $h(t)$ reprocessing, except when stated otherwise.

2. The Advanced Virgo detector during O2

Most of the detector characteristics relevant to calibration and described in [9, 10] for initial Virgo were still valid for Advanced Virgo during O2. They are briefly summarized in this section, with emphasis on the relevant modifications compared to the initial Virgo detector.

The optical configuration of Advanced Virgo, similar to initial Virgo, is a power-recycled interferometer with Fabry-Perot cavities as shown in figure 1. All the mirrors of the interferometer are suspended to a chain of pendulums for seismic isolation. The input beam is provided by a Nd:YAG laser with a wavelength $\lambda = 1064$ nm. The power at the input of the interferometer during O2 was about 14 W. The finesse of the 3-km long Fabry-Perot cavities in the arms has been increased to about 450. The readout of the interferometer main output signal was changed from heterodyne detection to homodyne (or DC) detection [2] but this has no impact on the calibration procedures since the used photodiode signal is proportional to the interferometer differential arm length in both cases. The interferometer arm length difference is controlled to keep a destructive interference at the interferometer output port, with a slight offset to allow for DC detection. In order to control the other degrees of freedom of the interferometer, the laser beam is phase modulated at a few tens MHz (6, 8 and 56 MHz among others) and the error signals are acquired and demodulated from photodiodes located at various places in the interferometer.

Data from the interferometer, like the optical power of various beams and the different control signals, are time series, recorded at 10 kHz or 20 kHz. The data are time-stamped using the Global Positioning System (GPS).

2.1. Mirror longitudinal actuation

Each Virgo mirror is suspended to a complex seismic isolation system. The bottom part is a double stage system with the so-called *marionette* as the first pendulum. The mirror is suspended to the marionette by pairs of thin steel wires. As a modification,

[‡] V1 for Virgo detector, O2 for O2 run, ReproXY with X the reprocessing number and Y a letter to tag specific cases if needed.

the reference mass is now suspended to the seismic filter above the marionette instead of being attached to the marionette as in initial Virgo. This makes the mechanical response of the pendulum more complex. But the resonances being below 1 Hz, the mechanical response above 10 Hz still has a simple $1/f^2$ behavior.

The position of the marionette and mirror is adjusted with electromagnetic actuators: permanent magnets are attached to the marionettes and on the back of the mirrors; a set of coils attached to the reference mass and whose current is driven by some electronic device allows to steer the suspended objects. The longitudinal controls are distributed between the marionette (up to a few tens of hertz) and the mirror (up to a few hundred hertz). Therefore, the marionette and mirror actuation responses need to be measured up to ~ 100 Hz and up to ~ 1 kHz respectively.

The actuation response includes the actuator itself and the response of the suspended mirror. The actuator is composed of a digital part, a Digital to Analog Converter (DAC), and the analog electronics which converts the DAC output voltage into a current flowing through the coil.

2.2. Sensing of the interferometer output power and control loops

The main output signal of the interferometer is the power at the dark port. It is sensed using two photodiodes. The photodiodes and their readout electronics have been changed with respect to initial Virgo. In particular, the main channel \mathcal{P}_{DC} , that measures the output power components from 0 to 10 kHz, is now obtained from the blend of two channels measured and digitized in two frequency bands. For the pick-off beam used for interferometer control, the demodulated channels, \mathcal{P}_{AC} , are extracted using digital demodulation [2], instead of analog demodulation in initial Virgo. However, these modifications do not impact the calibration procedures.

The principle of the longitudinal control loops is the same as described in [10] and sketched in figure 1.

3. Calibration of Advanced Virgo

To reconstruct the gravitational wave strain $h(t)$, we need to calibrate the sensing part (photodiode readout) and the actuators (coils acting on the mirrors and on their suspensions). More details on the procedures used can be found in the Virgo notes [11, 12].

Specific calibration data were taken a few days before Virgo joined the O2 run, every Tuesday during the run (about two hours of calibration each week), and finally during a measurement campaign over several days performed just after the end of O2. The results presented in this section are extracted from the whole dataset.

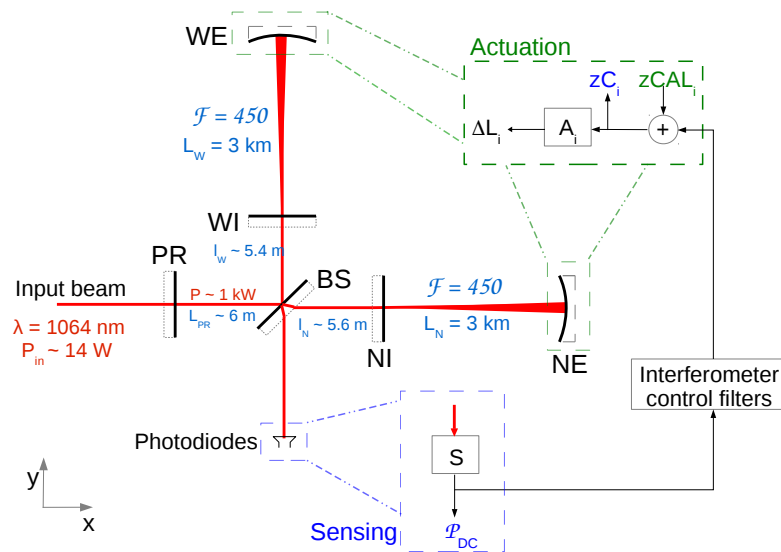


Figure 1. Configuration of the Advanced Virgo interferometer during O2 and sketch of the differential arm length control loop.

3.1. Timing and Sensing

The photodiode readout (sensing part of the control loop) is paced by a timing distribution system slaved to a main GPS receiver. This receiver provides a GPS timestamp and a clock distributed to all the digital electronic devices (ADC, DAC, real-time PCs, DSP boards, ...) to enslave their local clock and to time the data.

In order to estimate the absolute timing of the system, the 1 PPS (Pulse Per Second) clock signal of the current GPS receiver, already used for Virgo+ since 2008, has been compared to the 1 PPS of the initial Virgo GPS receiver [13]. No offset between the two systems was found within uncertainties of $4 \mu\text{s}$.

In addition, the Virgo clock has been compared to a clock provided by an independent atomic clock [14]. The atomic clock being free, it is expected to drift. A linear drift has been estimated over five days in September 2017, after O2, and is assumed to have been the same during O2. After removing this linear drift, the relative variations of the Virgo clock compared to the atomic clock were below $13 \mu\text{s}$ during O2. Note that part of such variations may still come from the atomic clock whose drift is not expected to be perfectly linear.

The full sensing chain of the output photodiodes is described in [15]. Using the clock signal from the main GPS receiver sent through a LED in front of the output photodiodes and recording the signals at 1 MHz, we have measured the position of the 1 PPS of the clock in the Virgo data. The measured delay of the sensing chain ($140 \pm 3 \mu\text{s}$) was in agreement with the expected value ($142 \pm 1 \mu\text{s}$).

From these uncertainties on the Virgo GPS absolute timing and on the photodiode readout chain delay, we have estimated a conservative systematic uncertainty of $20 \mu\text{s}$

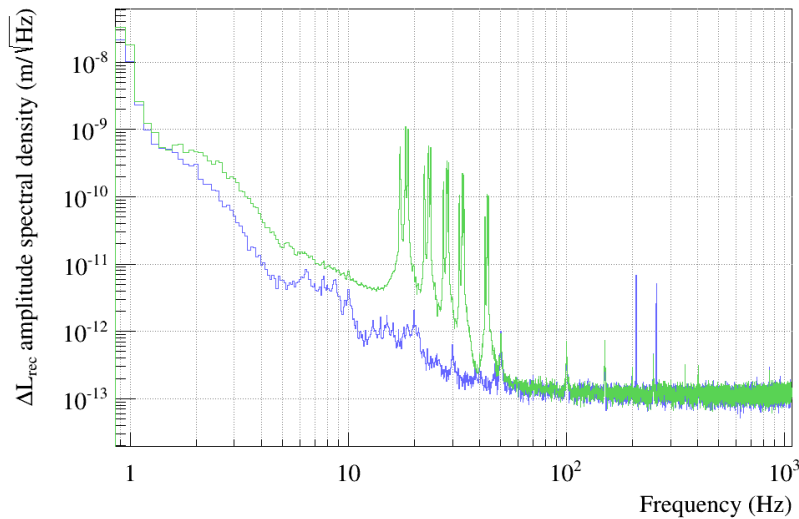


Figure 2. Amplitude spectral density of the reconstructed ΔL signal in the free Michelson configuration. Two dataset are shown with different sinewaves excitations applied on the mirror actuators. Green: five sinewaves are applied between 15 Hz and 45 Hz to each of the three mirrors. Blue: two sinewaves are applied between 200 Hz and 250 Hz to each of the three mirrors. The plots are made from two dataset lasting for 60 s.

on the absolute timing of the main output signal of the interferometer, \mathcal{P}_{DC} .

3.2. Calibration of the BS, NI and WI mirror actuators

The Advanced Virgo O2 calibration relies on several length references used in sequence. The first step is to calibrate the actuators of the input mirrors of each arm's cavity (NI and WI) and of the beamsplitter mirror (BS) in a free swinging short Michelson configuration using the main Virgo laser wavelength (1064 nm) as length etalon. In this configuration, from the interference fringes passing through the output photodiode, the differential arm length $\Delta L(t)$ is measured using a non-linear reconstruction that has been described in [9]. Applying known excitations to the mirror actuators and looking at their effect on the reconstructed ΔL , we can estimate the NI, WI and BS mirror actuator responses in meter per volt.

Typical amplitude spectral densities of the reconstructed ΔL signal are shown in figure 2. The blue line represents the sensitivity of the measurements: above 50 Hz, the sensitivity is dominated by the photodiode readout noise. The green line shows an example when some sinusoidal excitations were applied to the different mirror actuators: the applied excitations have signal-to-noise ratio of the order of few hundred up to 400 Hz. The NI, WI and BS mirror actuator responses have been measured up to 900 Hz.

3.3. Calibration of the NE and WE mirror actuators

Compared to initial Virgo, it is no more possible to calibrate directly the NE and WE end cavity mirror actuator with the free swinging Michelson technique, using asymmetric Michelson configurations, because the sensitivity for this measurement is reduced due to the lower transmittivity of the input mirrors and because the NE and WE actuators dynamics has been limited to only a Low Noise operation.

The method therefore uses the NI and WI mirror actuator responses, A_{in} , as the reference to measure the NE and WE mirror actuator responses A_{end} . With the full interferometer locked, one can compare the effect of known motions of the NI and WI mirrors on the dark fringe power to the effect of the known excitations of the NE and WE mirrors. This comparison, that we call calibration transfer, allows to estimate the NE and WE mirror actuator responses.

We can compute the transfer functions $TF_{in} = \mathcal{P}_{DC}/zCAL_{in}$ and $TF_{end} = \mathcal{P}_{DC}/zCAL_{end}$ between the dark fringe signal \mathcal{P}_{DC} and $zCAL_{in,end}$, the excitations injected on input or end mirrors of the arm cavities $zCAL_{in,end}$. We can then extract the end mirror actuators response A_{end} as:

$$A_{end} = A_{in} \times \frac{TF_{end}}{TF_{in}} \times \frac{R_{ITF,in}}{R_{ITF,end}} \quad (2)$$

where $R_{ITF,in}$ and $R_{ITF,end}$ are the interferometer optical response to the input and end mirrors motions (the responses are almost the same, but with a 0.37% difference in modulus and 10 μ s difference in phase [12]).

The actuators response can be decomposed into two parts: the pendulum mechanical response and the electronic response. NE and WE are suspended to a chain of anti-seismic suspension whose last stage can be modeled, in the frequency range of interest, as a simple pendulum (a complex pole at $f_{pend} = 0.6$ Hz with a quality factor $Q = 1000$, following a simple $1/f^2$ behavior above 10 Hz). Figure 3 shows the NE mirror actuator response normalized by this simple mechanical response model. The normalized modulus is mainly flat, within small deviations of $\pm 3\%$ coming from the electronics/actuator response. These small deviations are fitted (red curve) to provide the full actuator response model. The superposed green areas indicate the 1σ statistical uncertainties as function of frequency estimated using the fit covariance matrix. They are below 0.5% in modulus and 5 mrad in phase up to 800 Hz.

3.4. Calibration of the marionnetta actuators

The same transfer method is used in order to measure the Marionnetta actuator response. We compare the effect, on the dark fringe power, of a known mirror excitation motion to the effect of a known marionette actuator excitation. The marionette actuation response has been measured between 10 Hz and 200 Hz. More details on this part of the calibration can be found in [11].

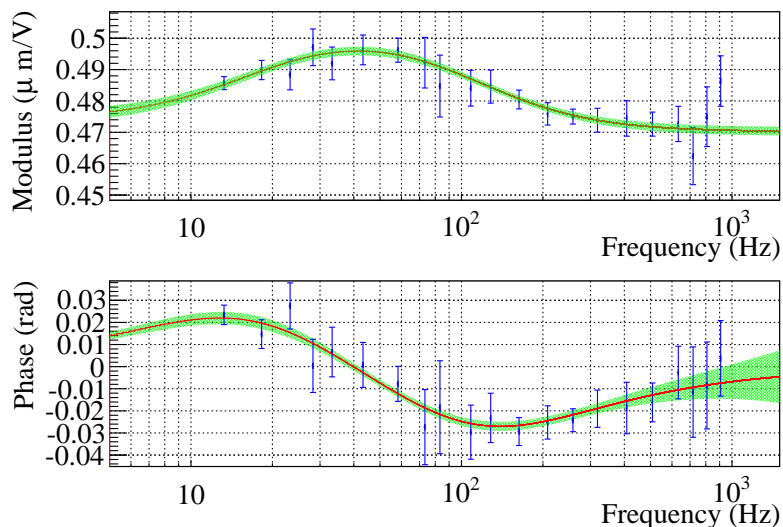


Figure 3. NE mirror actuator transfer function normalized by the mechanical transfer function and with the measured delay subtracted for a better visualization. Each blue point is an average over all the calibration measurements done at this frequency, with their 1σ statistical uncertainty. The red line is the fitted model for the (normalized) actuator response. The green filled area represents the 1σ statistical uncertainty as function of frequency.

3.5. Calibration of the PR mirror actuator

A similar transfer method is applied to measure the power-recycling mirror (PR) actuation response. It uses the cavity made of the PR and WI mirrors, using BS as a folding mirror, to compare the effect, on the photodiode error signal used in the control loop, of the known WI motion to the effect of a known PR actuator excitation. The PR actuation response has been measured between 10 Hz and 500 Hz. More details on this part of the calibration can be found in [11].

3.6. Uncertainties estimation

Each step of the calibration procedure contributes to the uncertainties in amplitude and phase of the actuator responses. Tables 1 and 2 give the total uncertainties for each actuators response (mirrors and marionettes respectively) and the breakdown of the various contributions.

The first line gives the statistical uncertainties estimated after all the measurements have been combined together to get the actuator response data and fit. The systematic uncertainties are given in the following lines. For each step, data taken at different times have been averaged together. However, for some of them, small time variations have been found: they are reported in the three next lines for the corresponding steps (either the initial measurement of the BS, NI or WI actuation, either the calibration transfers to NE, WE, PR mirror or marionettes). We found that, when normalizing

		NE mirror	WE mirror	BS mirror	PR mirror
Stat. uncertainty		0.5% (5 mrad)	0.5% (5 mrad)	1% (10 mrad)	2% (20 mrad)
Syst. uncert.	BS,NI,WI calib	0.4% (0 mrad)	0.4% (0 mrad)	0.2% (3 mrad)	0.4% (0 mrad)
	in to end transfer	0 (0 mrad)	0 (0.5 mrad)	–	–
	WI to PR transfer	–	–	–	0.3% (0 mrad)
Δf in normalization		0.2% at 20 Hz and 0.04% at 100 Hz (0 mrad)			
Readout delay		4 μ s			
Total uncertainty (linear sum)		1.1% 5 mrad 4 μ s	1.1% 5.5 mrad 4 μ s	1.4% 12 mrad 4 μ s	2.9% 20 mrad 4 μ s
Validity range		10-800 Hz	10-800 Hz	10-800 Hz	10-500 Hz

Table 1. Summary of the sources of statistical and systematic uncertainties on the mirror actuator models. For every source, the uncertainties on the modulus (phase) are given. The last lines give, for all the actuators, the sum of all the uncertainties reported in this table and their validity range. See text for details.

		NE mario.	WE mario.	BS mario.
Stat. uncertainty		2% (20 mrad)	2% (20 mrad)	0.5% (5 mrad)
Syst. uncert.	BS,NI,WI calib	0.4% (0 mrad)	0.4% (0 mrad)	0.2% (3 mrad)
	in to end transfer	0 (0 mrad)	0 (0.5 mrad)	–
	mir to mar transfer	0.3% (3 mrad)	0.2% (4 mrad)	0 (1 mrad)
Δf in normalization		0.2% at 20 Hz and 0.04% at 100 Hz (0 mrad)		
Readout delay		4 μ s		
Total uncertainty (linear sum)		2.9% 23 mrad 4 μ s	2.8% 24.5 mrad 4 μ s	0.9% 9 mrad 4 μ s
Validity range		10-100 Hz	10-100 Hz	10-80 Hz

Table 2. Summary of the sources of statistical and systematic uncertainties on the marionette actuator models. For every source, the uncertainties on the modulus (phase) are given. The last lines give, for all the actuators, the sum of all the uncertainties reported in this table and their validity range. See text for details.

the measured data by the simple pendulum model, some bias was introduced by using the frequency of the Fourier transform bin center, which was not exactly the injected frequency. This bias on the modulus, that decreases when the frequency increases, is also reported. Finally, the uncertainty estimated on the photodiode readout timing is given. The last lines of the tables summarize the total uncertainties obtained on the different actuator models and their validity range.

For NE and WE mirrors, a main source of uncertainty is the statistical error, mainly coming from the calibration transfers. Another main source of uncertainty on the modulus comes from the systematics due to the variation in time of the actuators response measured in the free Michelson configuration.

4. Reconstruction of the gravitational wave signal $h(t)$

Once the sensing chain and the control loop actuators are calibrated, we can reconstruct the gravitational wave signal $h(t)$. In this section, we report the principle of the $h(t)$ reconstruction, the main method used to estimate the systematic uncertainties and some consistency checks we performed. Finally, the systematic uncertainties obtained for the online $h(t)$ version and for the two post-O2 reprocessings are summarized. More details can be found in the Virgo notes [16, 17].

4.1. Principle

To compute $h(t)$, we remove from the dark fringe signal the contributions of the control signals by subtracting the corrections applied to the mirrors and we correct for the interferometer optical transfer function. This procedure does not correct the effect of control loops by applying a transfer function, but by subtracting their contributions. Therefore, some of the residual control signals, like the calibration lines (periodic excitations applied to the mirrors) are removed or reduced using this method.

Following the notations of figure 1, inputs are the measured dark fringe photodiode channel (\mathcal{P}_{DC}) and the correction channels (zC_i) sent to the mirror and marionette actuators, as well as the calibrated transfer functions for the photodiode readout and the different actuators. As in initial Virgo, the computation is done in the frequency-domain using fast Fourier transforms of 20 s with 10 s overlap. Calibration lines, applied as $zCAL_i$, are used to monitor the optical gain of the interferometer, that varies with the interferometer alignment for instance.

In addition, a frequency noise subtraction has been developed for the $h(t)$ reprocessings. Indeed, it arose that frequency noise was still present in the dark fringe signal during O2 and could be subtracted since it was also present in an auxiliary monitoring channel. First, the transfer function from the frequency noise to $h(t)$ is computed and assumed constant over some time period (defined in 4.2). Then, the frequency noise contribution, estimated from the auxiliary monitoring channel and the transfer function, is subtracted from $h(t)$.

The processing being done in the frequency domain, inverse fast Fourier transforms are used to obtain, in the time domain, the final $h(t)$ channel provided at both 20000 Hz and 16384 Hz sampling frequencies.

4.2. Main differences between the $h(t)$ versions

The Online $h(t)$ processing used the pre-O2 calibration models for the photodiode readout and the actuator responses. The optical response of the interferometer was approximated by a simple pole characterized by the Fabry-Perot cavity finesse. The Online version used a fixed value of the finesse set to 455, the value measured in 2016 with an error of $\pm 5\%$.

For the V1O2Repro1A $h(t)$ reprocessing, the three main changes have been to use the

post-O2 improved actuation calibration models based on the whole calibration dataset, to correct for a timing bias of 116 μs § and to subtract the frequency noise. For this reprocessing, the transfer function from frequency noise to $h(t)$ has been fit to the measurements and kept fixed for all the O2 data. In addition, some improvements have been done in the reconstruction code to reduce some glitches due to communication issues in the control signals that were found to happen during O2.

Finally, for the V1O2Repro2A $h(t)$ reprocessing, small adjustments of the calibration models were made (fix a bias of 0.37% in the modulus of the end mirrors, and add 10 μs in the interferometer optical response to the end mirror motions). The main modifications made on $h(t)$ processing have been:

- adapt the frequency noise subtraction transfer function every 500 s, monitoring the coupling of the frequency noise to $h(t)$,
- adjust the cavity finesse every 10 s to the value extracted from the phase of some calibration lines measured 10 s earlier.

As an additional improvement, we have been less sensitive to glitches by using median values instead of average values for the optical gain and finesse. Most of the results shown hereafter are computed from this V1O2Repro2A version.

Figure 4 compares the amplitude spectral densities of the three versions of $h(t)$. They are all very similar, but with some slight improvements of the reprocessing versions. It is mainly visible between 15 Hz and 30 Hz and between 150 Hz and 200 Hz, where the sensitivity has been improved with respect to the online $h(t)$ reconstruction, mainly thanks to the frequency noise subtraction. At frequencies above 3 kHz, the Advanced Virgo data are contaminated by a significant amount of spectral and transient noise. In the first reprocessing, the frequency noise subtraction was not well tuned at high frequency and added a slight excess of noise above 2 kHz that was no more present in the second reprocessing.

4.3. Uncertainty budget

To estimate the uncertainty on $h(t)$, including the possible bias of the reconstruction procedure, we have compared the reconstructed signal h_{rec} to a calibrated h_{inj} signal injected into the detector with the mirror electromagnetic actuators. Figure 5 shows the amplitude and the phase of the transfer function h_{rec}/h_{inj} where the coherence between both signals was higher than 0.95. Below 700 Hz, the comparison of h_{rec} and h_{inj} is within $\pm 4\%$ in amplitude and ± 35 mrad in phase, as shown by the red lines in the figure. In addition, the systematic uncertainty on the actuator model used to determine the reference h_{inj} signal is 1.1% in amplitude and 5 mrad in phase, and the systematic uncertainty on the timing is 20 μs .

§ This bias was due to a sign error for a 58 μs correction in the reconstruction configuration.

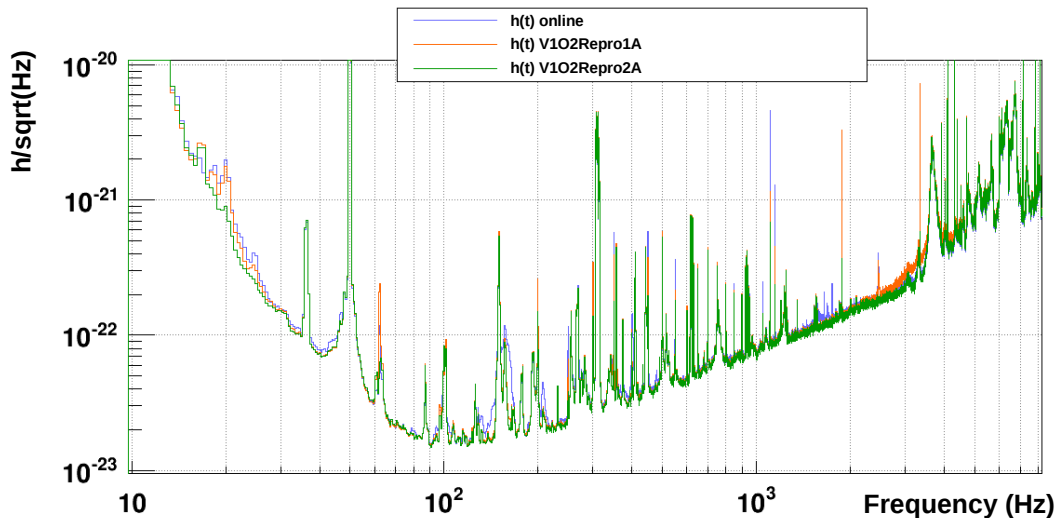
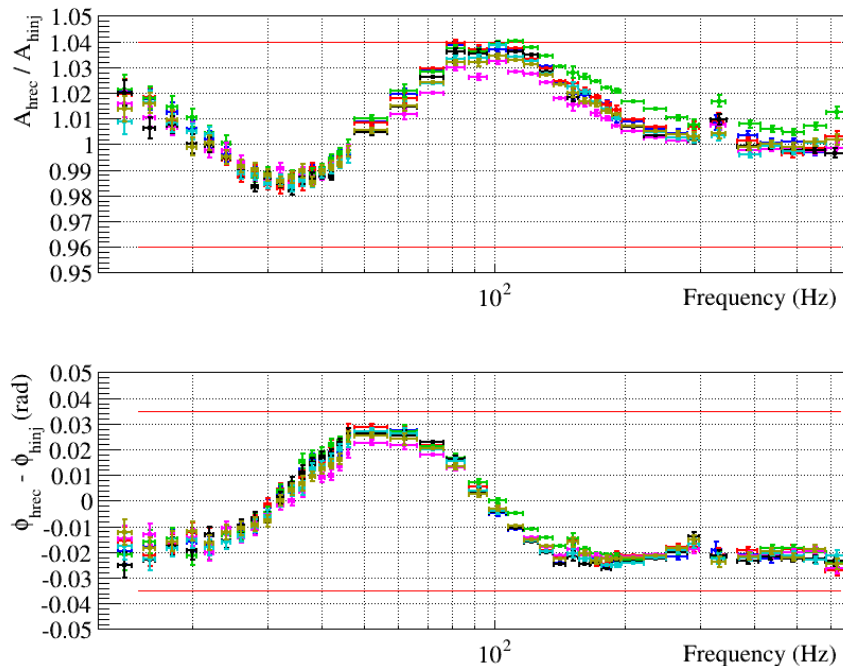


Figure 4. Amplitude spectral density of $h(t)$ Online (blue), V1O2Repro1A (orange) and V1O2Repro2A (green).

Due to the limited dynamic of the actuators, this method only applies up to 700 Hz. However the interferometer is basically kept free at high frequency since the contribution of the control signals amounts to only 4% of the dark fringe signal at 700 Hz and goes down at higher frequencies. Therefore, at high frequency, the h_{rec} signal is just the dark fringe signal corrected by the cavity response and the photodiode electronic chain response. As an additional check, the shot noise level has been measured at high frequency as the difference between the power measured by the two dark fringe photodiodes. As expected, it is flat, confirming that the bias introduced by the readout chain, and therefore the $h(t)$ uncertainty, is less than 4%. The $h(t)$ reconstruction is thus valid from 10 Hz up to the Nyquist frequency 8192 Hz (for the $h(t)$ channel sampled at 16384 kHz). The systematic uncertainty on the $h(t)$ amplitude and phase for the online first and second reprocessings are reported in table 3.

Below 700 Hz, the frequency-dependent deviation seen in the figure is larger than the uncertainty on h_{inj} coming from the actuators. It must thus be a real bias in the reconstructed $h(t)$ channel. These deviations being in the frequency range where the photodiode signal and the marionette and mirror control signals are all combined together to get $h(t)$, it is possible that small relative errors in gain or phase of the different sensing and actuation models sum-up and give rise to such a structure. Further investigations are on-going to really understand its origin.



x

Figure 5. Transfer function between the reconstructed $h(t)$ signal (h_{rec}) and the injected signals on NE mirror (h_{inj}). The different colors correspond to various sets of injections during the O2 run. The comparison of h_{rec} and h_{inj} is within $\pm 4\%$ in amplitude and ± 35 mrad in phase as shown by the red lines.

$h(t)$ version	Amplitude uncertainty (%)	Phase uncertainty (rad)	Timing bias
Online	+14/ - 8	$100 \times 10^{-3} + 2\pi f(20 \times 10^{-6})$	116 μ s
V1O2Repro1A	± 8	$50 \times 10^{-3} + 2\pi f(20 \times 10^{-6})$	0
V1O2Repro2A	± 5.1	$40 \times 10^{-3} + 2\pi f(20 \times 10^{-6})$	0

Table 3. Summary of the uncertainties estimated for the three versions of $h(t)$ reconstructed for the O2 run. For the Online version, the timing bias indicate that the reconstructed $h(t)$ was too late with respect to the *true* $h(t)$. It can either be corrected for when using the $h(t)$ channel or added linearly to the timing error. The validity range is from 10 Hz to 8 kHz for the three versions.

5. Consistency checks with the photon calibrator (PCal)

There are limitations in the way we can check the reconstructed $h(t)$ with respect to a differential arm length signal injected through the electromagnetic actuators of the mirrors because the models used in the reconstruction of $h(t)$ are derived from the calibration procedure and an error on the actuator gains, larger than the computed uncertainties, would not be detected with this method.

Performing a similar check but with another actuator, independently calibrated, allows to cross-check the results described in the previous sections. This is provided by inducing mirror displacements with a photon calibrator (PCal).

5.1. Principle of the photon calibrator

The PCal is based on a 3 W laser with a wavelength $\lambda = 1047$ nm used to apply a force on a mirror by radiation pressure. So far, in Advanced Virgo, one PCal was installed to push the WE mirror from the inner side of the Fabry-Perot cavity. The force F applied on the mirror is longitudinal:

$$F = \frac{2 \cos(i)}{c} P_{ref} \quad (3)$$

where c is the speed of light in vacuum, i the angle of incidence of the laser on the mirror and P_{ref} the power of the PCal beam reflected by the WE mirror. An excitation ΔF is applied by modulating the power of the PCal laser up to a few kHz, resulting in a mirror motion Δx which verifies:

$$\Delta x = -\frac{1}{m} \frac{1}{(2\pi f)^2} \times \Delta F = -\frac{2 \cos(i)}{mc} \frac{\Delta P_{ref}(t)}{(2\pi f)^2} \quad (4)$$

with m is the mass of the mirror and f the frequency of the sinusoidal force of amplitude ΔF . This equation holds for frequencies above 10 Hz, well above the resonant frequency of the pendulum. This method enables us to compare an equivalent strain h_{pcal} injected in the interferometer through the PCal with the reconstructed signal h_{rec} . More details on the setup can be found in [18].

5.2. Sign of $h(t)$

PCal injections can be used to establish the sign of $h(t)$, defined in equation 1, since we know that the variation δL_W (i.e. δL_y) when the laser beam of the PCal pushes the mirror is the opposite of PCal power measurement P_{ref} . Therefore, if the phase of the transfer function from the PCal power applied on WE mirror, P_{ref} , to $h(t)$ is equal to 0, equation 1 is verified and thus the sign of $h(t)$ is correct. This assumes that the photodiode output is recorded as a positive quantity which can be easily checked since there is a DC offset on the PCal laser power. This is indeed what we measure.

5.3. Partial confirmation of $h(t)$ systematic uncertainties with the PCal

The transfer function of the reconstructed line amplitudes h_{rec} over the injected line amplitudes with the PCal h_{pcal} is shown on figure 6. Since the calibration of the PCal beam power measurement was not stable during O2, with variations^{||} of $\sim 20\%$, the different transfer functions h_{rec}/h_{PCal} measured during O2 have been normalized in order to have a modulus of 1 at the 356 Hz PCal calibration line. In addition, since the PCal beam hits the center of the WE mirror, it excites the drum mode of the mirror. This modifies the simple mechanical response described in equation 4, adding a notch around 2 kHz (see [10] for more details). The left plot of figure 6 shows the normalized amplitude ratio and the 2 kHz notch that was fitted on the data. The right plot shows

^{||} Post-run analysis have shown that the system was suffering from PCal beam polarization changes and some photodiode saturations.

the phase difference, where the drum mode excitation has no impact as long as the measurements are below the notch frequency.

From the normalized modulus plot, we cannot have an absolute verification of the amplitude of the reconstructed $h(t)$. However, the overall relative amplitude can be checked. Once normalized, they lie within the $\pm 4\%$ error band that is used for the calibration uncertainty. The important point is that the frequency-dependent deviation is similar to the one found with the electro-magnetic actuators shown in figure 5. This highlights that the deviation is a real bias in the reconstructed $h(t)$ signal. This will be further investigated with future data taking.

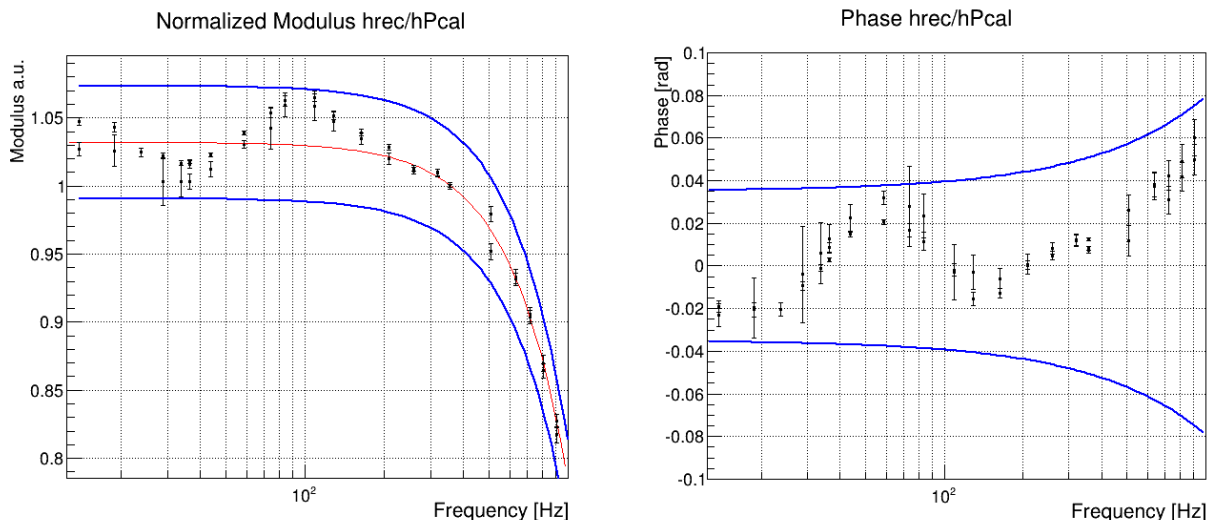


Figure 6. Left plot represents the normalized transfer function between the reconstructed lines amplitude and the PCal injected lines amplitude. The data points are fitted with a notch around 2 kHz and remain in the $\pm 4\%$ error band. Right plot shows the phase of this transfer function with an error band of $\pm 35 \pm 2\pi f \times 7e-3$ mrad.

The blue lines on the phase difference correspond to an error band of ± 35 mrad uncertainty and a delay of $\pm 7 \mu\text{s}$ which is the sum of the timing uncertainties of the PCal photodiode ($3 \mu\text{s}$) and of the dark fringe photodiode ($4 \mu\text{s}$). The timing of the PCal photodiode readout has been calibrated with a GPS clock signal, using the same method as described in section 3.1. The phase of the transfer function h_{rec}/h_{PCal} lies within this error band.

To conclude, the comparison of the reconstructed $h(t)$ with the PCal injections has validated the sign of $h(t)$ and the estimated uncertainties on the phase of $h(t)$. About the amplitude, while it cannot be used to validate the uncertainties, the fact that the frequency variation of the comparison are similar with both PCal and the standard mirror actuators gives extra confidence in the measurements.

6. Conclusion

We have described the Advanced Virgo calibration and the $h(t)$ reconstruction procedures used in the O2 observation run in August 2017. Using the interferometer laser wavelength as primary etalon and a calibration transfer procedure, we could calibrate the BS, NE, WE and PR mirrors and marionetta actuators. They are important inputs for the $h(t)$ reconstruction that subtracts from the dark fringe signal the control signals applied on the actuators. The sources of systematic uncertainties have been described as well as the method to estimate the uncertainties on the reconstructed $h(t)$ channel summarized in table 3, reaching 5.1% in amplitude and 40 mrad and 20 μ s in phase and timing for the latest reprocessing version.

Following the first Virgo detections of gravitational wave signals during O2, the LIGO and Virgo detectors are being improved and commissioned in preparation of the run O3. With this three-detector network of improving sensitivity, there are strong prospects of many more detections with increasing signal-to-noise ratio for the strongest events. In this context, the reconstruction uncertainties must be reduced down to the percent level in the coming years in order not to contribute to the source parameter estimation uncertainties.

To achieve this goal, work is on-going to better calibrate the mirror actuators improving the photon calibrator setup and installing a new calibration hardware, called Newtonian calibrator, that has shown good and consistent results in recent tests [19]. Due to the very tight schedule for the O2 run, time dedicated to calibration was very limited. In order to reduce uncertainties and to refine the models used for the online reconstruction, it is planned to keep the interferometer in a stable configuration with more calibration measurements before the start of future observation runs.

In the $h(t)$ reconstruction algorithm, studies to improve and adapt the optical models following the interferometer configuration are being pursued. For O2, the bias found on the $h(t)$ signal has been included in the systematic uncertainties. We plan to reduce it in the future by using a more accurate modelling of all actuator mirrors and optical responses, and if needed by correcting the measured bias in the reconstructed $h(t)$ channel.

Acknowledgements

The authors gratefully acknowledge the Italian Istituto Nazionale di Fisica Nucleare (INFN), the French Centre National de la Recherche Scientifique (CNRS) and the Foundation for Fundamental Research on Matter supported by the Netherlands Organisation for Scientific Research, for the construction and operation of the Virgo detector and the creation and support of the EGO consortium.

References

- [1] Accadia T, et al (Virgo Collaboration) 2012 The AdV Technical Design Report URL <https://arxiv.org/abs/1206.0341>

- [//tds.virgo-gw.eu/ql/?c=8940](https://tds.virgo-gw.eu/ql/?c=8940)
- [2] Acernese F *et al.* (Virgo collaboration) 2015 *Class. Quant. Grav.* **32** 024001 (*Preprint* 1408.3978)
 - [3] Aasi J *et al.* (LIGO Scientific Collaboration) 2015 *Classical and Quantum Gravity* **32** 074001 URL <http://stacks.iop.org/0264-9381/32/i=7/a=074001>
 - [4] Viets A *et al.* 2018 *Class. Quantum Grav.* **35** 095015 (*Preprint* 1710.09973)
 - [5] Abbott B P *et al.* (LIGO Scientific Collaboration and Virgo Collaboration) 2017 *Phys. Rev. Lett.* **119**(14) 141101 URL <https://link.aps.org/doi/10.1103/PhysRevLett.119.141101>
 - [6] Abbott B P *et al.* (LIGO Scientific Collaboration and Virgo Collaboration) 2017 *Phys. Rev. Lett.* **119**(16) 161101 URL <https://link.aps.org/doi/10.1103/PhysRevLett.119.161101>
 - [7] Abbott B *et al.* (LIGO Scientific Collaboration and Virgo Collaboration) 2018 *submitted* (*Preprint* 1805.11579) URL <https://arxiv.org/abs/1805.11579>
 - [8] Abbott B and other (KAGRA Collaboration, LIGO Scientific Collaboration and Virgo collaboration) 2018 *Living Rev. Relativ.* **21** (*Preprint* 1304.0670)
 - [9] Accadia T *et al.* (Virgo Collaboration) 2011 *Class. Quant. Grav.* **28** 025005 (*Preprint* 1009.5190)
 - [10] Accadia T *et al.* (Virgo Collaboration) 2014 *Class. Quant. Grav.* **31** 165013 (*Preprint* 1401.6066)
 - [11] D Estevez, V Germain, F Marion, B Mours, L Rolland, D Verkindt 2017 Advanced Virgo calibration for O2: photodiode sensing and mirror and marionette actuator responses URL <https://tds.virgo-gw.eu/ql/?c=12640>
 - [12] D Estevez, F Marion, B Mours, L Rolland, D Verkindt 2018 Advanced Virgo calibration for O2: update for h(t) reconstruction reprocessing V1O2Repro2 URL <https://tds.virgo-gw.eu/ql/?c=12902>
 - [13] L Rolland, N Letendre, A Masserot, B Mours 2010 Stability of the timing system during VSR2 URL <https://tds.virgo-gw.eu/ql/?c=7509>
 - [14] D Estevez, V Germain, F Marion, A Masserot, B Mours, L Rolland, D Verkindt 2017 Check of the DAQ timing during O2 URL <https://tds.virgo-gw.eu/ql/?c=12641>
 - [15] D Estevez, V Germain, F Marion, A Masserot, B Mours, L Rolland, D Verkindt 2017 Advanced Virgo SDB2 B1/B1p timing for O2 URL <https://tds.virgo-gw.eu/ql/?c=12707>
 - [16] D Estevez, F Marion, B Mours, L Rolland, D Verkindt 2018 V1O2Repro1A h(t) reprocessing for Virgo O2 data URL <https://tds.virgo-gw.eu/ql/?c=13253>
 - [17] D Estevez, F Marion, B Mours, L Rolland, D Verkindt 2018 V1O2Repro2A h(t) reprocessing for Virgo O2 data URL <https://tds.virgo-gw.eu/ql/?c=13254>
 - [18] Rolland L *et al.* 2015 *Conceptual design of Advanced Virgo photon calibration* VIR-0013A-15 URL <https://tds.virgo-gw.eu/ql/?c=10722>
 - [19] Estevez D *et al.* First Tests of a Newtonian Calibrator on an Interferometer Gravitational Wave Detector submitted to CQG (*Preprint* arXiv:1806.06572)